Creep and fatigue damage assessment for molten-salt central receivers

Marta Laporte-Azcué[1], Pedro Ángel González-Gómez[1], María de los Reyes Rodríguez-Sánchez[1] and Domingo Santana[1]

[1] Energy Systems Engineering Group (ISE), Department of Thermal and Fluid Engineering, University Carlos III of Madrid, Leganés (Spain)

Abstract

The receiver of the solar power tower plants is one of the subsystems under extremely demanding working conditions: the high heat fluxes concentrated onto its surface by the heliostat field are responsible for the receiver tubes high temepratures and thermal and mechanical stresses. On the one hand, the receiver tubes suffer from creep damage during hold periods under these conditions. On the other hand, the cyclic operation of the receiver at these high temperatures and stresses, caused by cloud passages and night periods interruptions, is responsible for the fatigue damage on the tubes. Yet, the lack of consensus in the molten-salt receiver field of study, with works neglecting either one damage mechanism or the other, motivates this study, in which a preliminary analysis on the creep and fatigue damages share in a molten-salt central receiver is carried out for different days of the year and direct normal irradiance configurations. The goal is to determine the possible damage mechanism trends during the receiver operation going from clear days to others with intermittent interruptions at high frequencies. The results show that, with a reasonable control of the receiver operation, the creep is the most relevant cause of receiver damage, opposite to fatigue, which would only be a matter of concern during days with high intermittent DNI and no regard for the flux incident of the receiver.

Keywords: External central receiver, Creep-fatigue, Lifetime, Transient operation.

1. Introduction

Solar power tower plant receivers are one of the most critical subsystems of these facilities, being subjected to high non-uniform heat fluxes coming from the heliostat field, which result in high tube temperatures as well as high thermal and mechanical stresses. Under these conditions, the receiver transient operation, caused by the daily cycles and cloud passages, is responsible for fatigue damage on these tubes, while during hold periods, the creep damage becomes a concening damage mechanism.

Early-day analysis of the damage inflicted to molten-salt receivers during their regular operation were based on the ASME Code Case N-47 (American Society of Mechanical Engineers, 1980), suitable for nuclear applications. These studies were mainly focused on the fatigue damage caused by the receiver cyclic operation (Grossman and Jones, 1990) rather than the creep damage one (hold periods at high temprature), with some studies even considering the creep damage negligible (Babcock & Wilcox Company, 1984; Kistler, 1987). The N-47 was simplified by Berman et al. (1979) to make it more suitable for its application in concentrating solar power technologies; such simplification was followed in the work of Narayanan et al. (1985), regarding both the creep and fatigue damages. However, the creep assessment is considered a very simplified one. More recently and also in the field of the molten-salts receiver, the creep-fatigue analysis performed by González-Gómez et al. (2021), which introduced a methodology to take into account commonly-disregarded aspects such as the stress relaxation or the plasticity effects, resulted in greater creep, with fatigue being negligible, although it was performed for clear-sky conditions.

In addition, recent works contemplating the use of alternative heat transfer fluids (HTFs), which are oriented to an operation with higher temperatures than molten-salts, showed a consensus in the fact that the creep damage mechanisim was the most prominent one: Fork et al. (2012) studied an air receiver, Neises et al. (2014) a receiver using sCO_2 as HTF and Conroy et al., (2018) analysed multiple aspects of a billboard sodium receiver.

Thus, in sight of the gap found for the range of temperatures of molten-salt receivers between the results of early-day works, wich used quite simplified approaches, and the more recent ones, wich deal with a more detailed creep-damage calculation, this work aims to obtain preliminary results on the investigation of the creep and fatigue damages share under the transient conditions.

doi:10.18086/swc.2021.13.02 Available at http://proceedings.ises.org

2. Methodology

The calculation procedure for the receiver analysis comprehends several models that deal from the receiver interaction with the heliostat field to the damages and lifetime analysis of its tubes. The required models for such integral analysis are detailed below.

The heat flux distribution on the receiver is obtained with the optical model proposed by Sánchez-González and Santana (2015), where the heliostat field aiming strategy, *k*, is selected: it can be from an equatorial strategy, (the target is the middle length of the receiver), to an open one (aiming towards both receiver ends). The equatorial strategy results in high peak fluxes, providing a greater optical efficiency and power production, although such fluxes could damage the receiver tubes in excess; on the other hand, the open strategies decrease the peak flux but result in a lower efficiency. In addition, a minimum solar height of 10° is required (Falcone, 1986) to evaluate the flux on the receiver. The goal is to avoid great optical losses in the heliostat field due to shading and blocking of heliostats or the cosine effect, which are more prominent near sunrise and sunset. Hence, the heliostat field aiming strategy is selected as equatorial as possible for the time intervals in which the clear-sky days under study are discretized. Nevertheless, the film temperature and the stress reset limit (Becht IV, 2011) are watched in the models presented below in order to avoid the tubes accelerated corrosion and to guarantee the global stress relaxation, respectively, which may require modifying the aiming strategy as the day progresses in order to not surpass these limits at any time. This results in the scheduled heliostat field aiming strategy for the clear day. During periods of lower DNI with respect to the expected clear-sky one, the heliostat field aiming strategy remains the same as the scheduled for the clear day, given the uncertainty that characterizes the cloud transients that decrease such DNI.

Then, the thermal model for the receiver is the one proposed by Rodríguez-Sánchez et al. (2014) which allows to obtain the tubes temperatures, including the film temperature that should be watched. In such thermal model, the receiver tubes are discretized in axial and circumferential divisions, and just one tube representative per panel is regarded. Two modes are contemplated regarding the thermal model: during clear-sky conditions, the HTF mass flow is adjusted so its outlet temperature meets the desired value (565°C), while during transient periods the mass flow used is the clear-sky scheduled ones and the HTF outlet temperature fluctuates in lower values than the objective one.

With the tubes temperatures, the elastic stresses and strains (σ_{eq}^{E}, ε_{eq}^{E}) are calculated with the model presented by Laporte-Azcué et al. (2020), which takes into account the temperature dependence of the tube material properties, providing more accurate results than the case of constant properties. Here it must be checked that the elastic stresses are below the stress reset limit:

$$S_{SR} = S_{y,cold} + S_H, \qquad \text{(eq.1)}$$

where $S_{y,cold}$ is the yield strength at room temperature and S_H is the hot relaxation strength, typically taken as 1.25 times the allowable stress, *S*, established by the ASME BPVC, Section II Part D (American Society of Mechanical Engineers, 2010). In addition, since the stress reset limit is just below the twice yield strength, the plastic shakedown regime is also avoided.

Lastly, the damage model proposed by (González-Gómez et al., 2021) is employed. The initial step is to obtain the elastic-plastic stresses and strains (σ_{eq}, ε_{eq}) by means of the elastic ones. Then, the stress relaxation of the tubes is also considered for a stabilization time, t_{stab}, of 30 hours (González-Gómez et al., 2021) since the global stress relaxation phenomenon is guaranteed by not surpassing the stress reset limit:

$$\sigma_{relax} = \sigma_{eq} - E\left[\left(\sigma_{eq}/E\right)^{1-n_r} - (1-n_r)AE^{n_r}\exp(-Q/(RT))\frac{t_{stab}^{m+1}}{m+1}\right]^{\frac{1}{1-n_r}}. \qquad \text{(eq.2)}$$

Here *Q* stands for the creep activation energy (J/mol), *R* is the ideal gases constant (J/(molK)) and *E* is the Young modulus (Pa). The *m* coefficient is the creep exponent that, when set to zero gives a simple Norton equation, allowing to consider the secondary creep rates, n_r is the creep-strain model coefficient and *A* is the stress relaxation constant ($1/(\mathrm{Pa}^{n_r}\mathrm{s})$). The stabilization time is expressed in seconds in eq. 2.

Thus, the creep stress results as

$$\sigma_c = \left(\sigma_{eq} - \sigma_{relax}\right)/C', \qquad \text{(eq.3)}$$

where *C'* is a safety factor set as 0.9, suitable for inelastic analysis of CSP technologies (Barua et al., 2020). If, as the result of such coefficient, the creep stress is greater than the equivalent one, the latter is taken instead in order to

avoid an excessive level of conservatism. The rupture time is then calculated with the Mendelson-Roberts-Manson parametrization:

$$\log_{10}(t_R) = \beta_0 + \beta_1 \frac{1}{T} + \beta_2 \log_{10}(\sigma_c) + \beta_3 \log_{10}(\sigma_c) \frac{1}{T} \quad \text{(eq.4)}$$

Being T the tubes temperature in Kelvin and β the coefficients of the parametrization, which depend on the material selected (Laporte-Azcué et al., 2021a). In eq. 4 the creep stress is introduced in MPa.

Then, the creep damage during day i is obtained as the summation of the ratios between the duration of the time intervals at which the day is discretized (a total of J) over the number of hours resulting from the rupture time calculation at every time interval:

$$d_{c,i} = \sum_{j=1}^{J_i} \frac{\Delta t}{t_{R,j}}. \quad \text{(eq.5)}$$

On the other hand, the fatigue damage is due to the M fatigue cycles during the day, N, and the number of allowable cycles in which these strain ranges result individually, N_a:

$$d_{f,i} = \sum_{m=1}^{M,i} \frac{N_m}{N_{a,m}}. \quad \text{(eq.6)}$$

The number of allowable cycles of the material depends on the equivalent elastic-plastic strain range as:

$$\frac{\Delta\varepsilon_{eq}}{2} = \frac{\Delta\varepsilon_{eq}^E}{2} + \frac{\Delta\varepsilon_{eq}^P}{2} = \frac{\sigma_f'}{E} N_a^{-c1} + \varepsilon_f' N_a^{-c_2}. \quad \text{(eq.7)}$$

The exponents and coefficients of such expression also depend on the material used. In order to take into account the possible creep-fatigue interaction effects, such N_a is modified with a reduction factor of 4, prior its use in Equation 6 (Radke et al., 2017). Moreover, the strain range of Equation 7 is altered by a x2 factor and constitutes a way of taking into account the effects of the load history, the size, the material variability and the surface finish of the specimen under study (O. K., Chopra; W. J., 2003; Radke et al., 2017).

With all of the above, the receiver lifetime is obtained by means of the equivalent operating days (EODs), calculated for a single day as:

$$D_L = d_c\, EODs + d_f\, EODs \rightarrow EODs = \frac{D_L}{d_c + d_f}\,, \quad \text{(eq.8)}$$

which satisfies that the damage limit, D_L, is not surpassed by the summation of the total creep and fatigue damages ($D_L \geq D_c + D_f$). In this case, the linear damage summation model has been considered, which is equivalent to a linear interaction of the creep and fatigue damages, with their sum always being equal to one.

The interaction among the models used and the thermal and mechanical limitations involving them which have been regarded are presented in Figure 1.

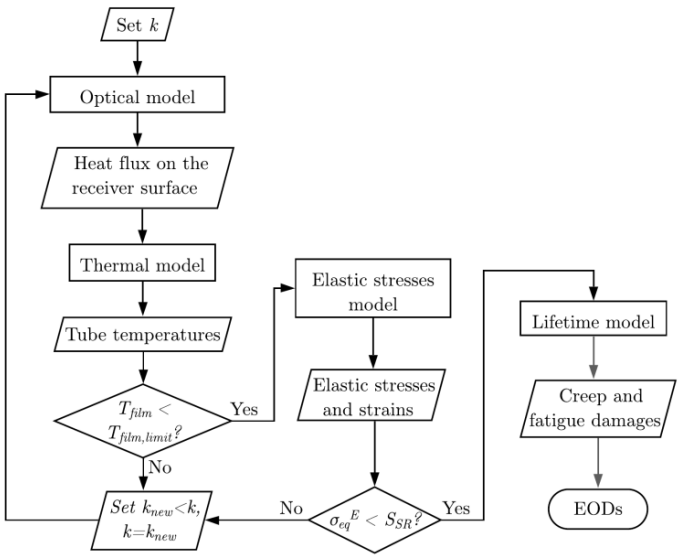

Fig. 1: Calculation procedure with the models employed.

3. System description

3.1. Heliostat field and receiver configuration

The heliostat field selected is located in Seville, Spain at a latitude of 37.56°. Its layout corresponds to the Gemasolar plant one, with 2,650 heliostats of 115.8 m^2 of effective mirror surface each, which gives a 306,605 m^2 of mirror area in total (Burgaleta et al., 2011).

On the other hand, an external tubular central receiver of cylindrical shape, depicted in Figure 2, is the main object of this study. Such receiver is constituted by 18 identical panels that surround the cylindrical frame of 8.5 m of diameter holding them, which is placed at the top of a 130 m height tower. The panels are constituted by vertically disposed tubes of length 10.5 m, their external diameter is 2.24 cm, being 1.2 mm thick. Their separation within a certain panel is initially set at the 8% of their external diameter, although such distance is adjusted so an integer number of tubes fit while being evenly spaced. Thus, giving the number of panels, the receiver frame diameter, the tubes outer diameter and their separation, the number of tubes per panel results in 61. These tubes are coated with a black Pyromark painting in order to increase their absorptivity, while the base frame –that behaves as a refractory wall– is covered with a high reflectivity paint so the greatest amount of radiation is reflected to the tubes. The material selected in this work for the tubes manufacturing is Haynes 230 since it has been proven to be one of the best alternatives in terms of endurance and thermal power/cost ratio (Laporte-Azcué et al., 2021a), outperforming other materials used in the field, such as alloy 316H, Inconel 625 or Incoloy 800H; in addition, it showed a linear interaction of the total creep and fatigue damages, as assumed in the linear damage summation model, in the experiments performed by Chen et al. (2013). Haynes 230 thermal and mechanical properties are available as temperature dependent in the ASME BPVC Section II, Part D (American Society of Mechanical Engineers, 2010), while its creep and fatigue damage coefficients are compiled in (González-Gómez et al., 2021), which are essential to undertake the receiver lifetime analysis. The tubes are guided by a series of welded supports, called clips, in order to avoid their excessive deflection, which could cause collision between adjacent tubes. For this study, an infinite number of clips is selected, equivalent to the generalized plane strain conditions.

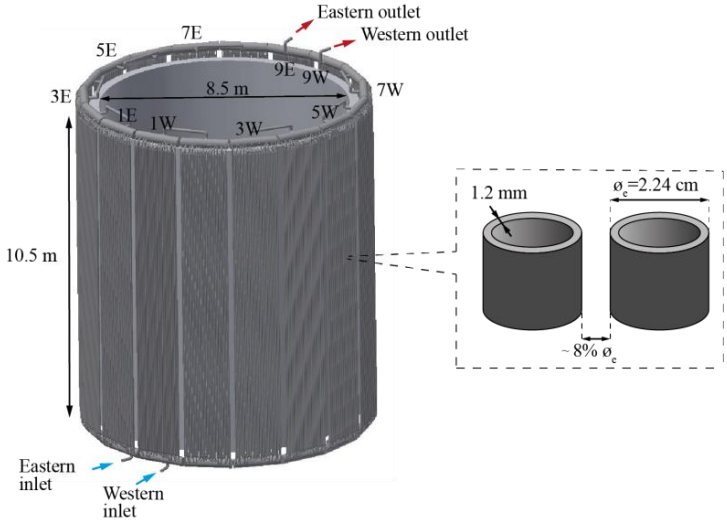

Fig 2: Schematic representation of the receiver under study

The solar salt ($NaNO_3$-KNO_3) used as HTF is divided into two parallel flow paths, symmetrical with respect the N-S direction, with the inlet of the cold fluid in the northern panels and the outlet of the hot HTF being located in the southern ones (panels 9E and 9W for each flow path, as depicted in Figure 2). The HTF flows through the panels of each path in a serpentine-like way, alternating upwards and downwards flow. The combination of HTF and tube material selected results in a maximum allowable film temperature of 650 °C (McConohy and Kruizenga, 2014).

3.2. Days under study and direct normal irradiance cases

Three days are selected to perform the study: the spring equinox (Julian day 81), the summer solstice (day 172) and the winter one (355). Their clear-sky DNI (Figure 3) is obtained according to the Daneshyar-Paltridge-Proctor model (Reno et al., 2012). The different start and final time instants depicted for each day is related to the 10° sun altitude condition set in the heliostat field optical model described in Section 2.

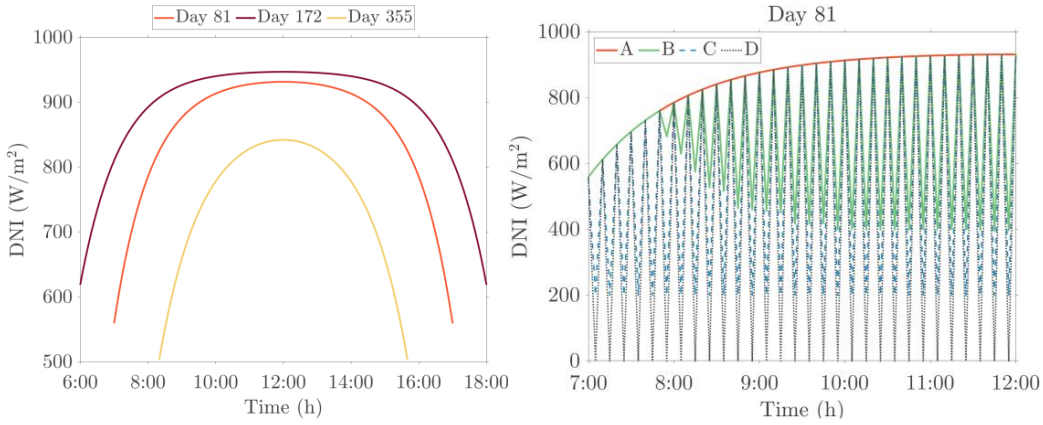

Fig. 3: Clear-sky DNI for the days analyzed (left) and DNI cases during the spring equinox morning hours (right).

For the scheduled aiming strategy, the receiver operation is subject to a minimum heat flux on the receiver equal or above 40 kw/m^2. On the other hand, despite control operation algorithms are not contemplated in this preliminary analysis, the receiver is kept in preheating conditions if the average heat flux with the scheduled aiming strategy is also equal or above 40 kW/m^2; that way, the range between 12 and 36 kW/m^2 (Vant-Hull, 2002) could be achieved with aiming strategies oriented to the preheat mode. Thus, the contribution of the creep and fatigue damages is addressed by studying the three selected days under four different DNI scenarios, depicted in Figure 3 (right side) for the spring equinox:

- The first one, case A, is the clear sky day.
- Then, to properly sense the fatigue damage, the DNI fluctuates as the time intervals progress between the clear-sky one and the minimum DNI that guarantees the receiver operation conditions (case B).
- Case C is under a DNI going alternatively between the clear-sky one and a DNI below the operation conditions but guaranteeing the preheat ones.
- Lastly, as an extreme fatigue situation, a day with its DNI fluctuating between the clear-sky DNI and zero, case D.

For these scenarios, the days have been discretized in time intervals of 5 minutes, since they offer a good compromise between computational cost and accuracy in the receiver lifetime estimation (Laporte-Azcué et al., 2021b).

4. Results and discussion

The maximum creep and fatigue damages for the eastern flow path of the receiver are presented for all its panels in Figures 4 and 5, respectively. The western half is omitted since the DNIs studied are symmetrical with respect solar-noon, resulting in the same outcome for both receiver halves.

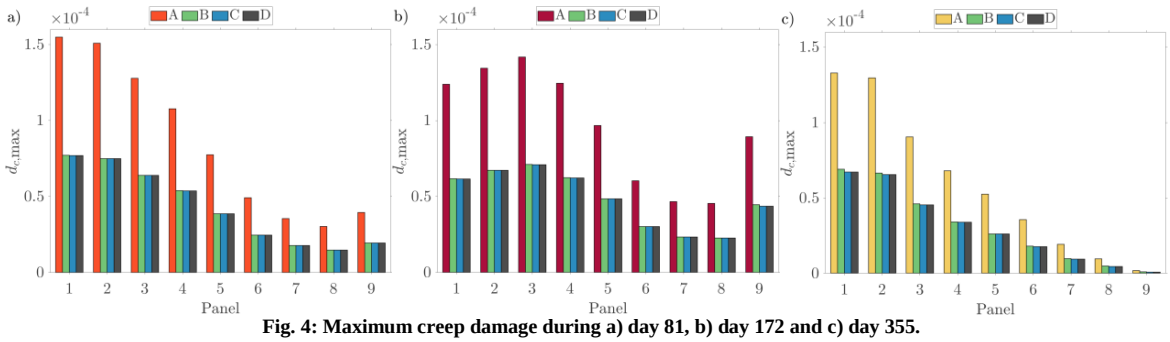

Fig. 4: Maximum creep damage during a) day 81, b) day 172 and c) day 355.

Regarding the $d_{c,max}$, the clear-sky scenario is the critical one, with the creep damage for cases B, C and D dropping almost the same amount for the three selected days (Spring equinox, Winter solstice and Summer solstice), around half of the clear-sky creep damage. These two facts are particularly relevant since it means that the creep damage during situations far from the clear-sky conditions does not depend on the operation mode and is almost negligible in these three scenarios: whether the receiver operates with periods of a minimum heat flux at the verge of ceasing its operation, or periods where is kept preheating, the creep damage is negligible since the total during the day is similar to one for the case with those periods resulting in the receiver completely shut down.

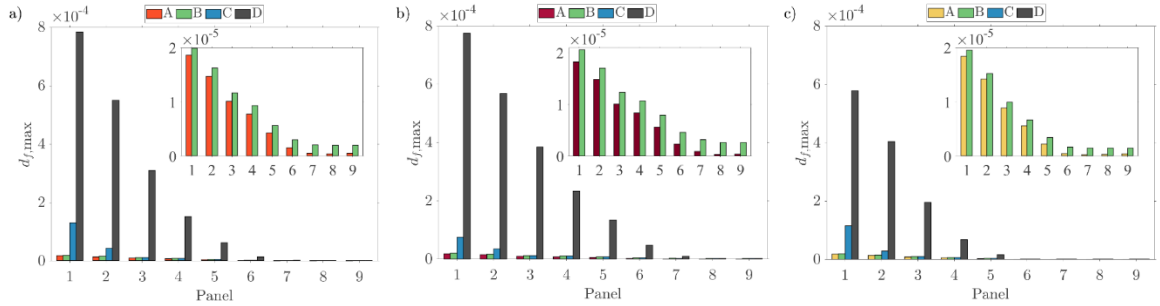

Fig. 5: Maximum fatigue damage during a) day 81, b) day 172 and c) day 355. Conclusions

On the contrary, Figure 5 shows that the $d_{f,\max}$ of the case with extreme fluctuations (D) is one order of magnitude greater than the one obtained for cases A and B and over 5 times greater than case C; moreover, such fatigue damage is also one order of magnitude greater than its corresponding creep damage. In case C, the $d_{f,\max}$ is twice its $d_{c,\max}$. Lastly, for cases A and B, it is one order of magnitude lower than the creep damage. Thus, looking at the case B, with the same number of fatigue cycles than the cases C and D, the setting of the minimum heat flux on the receiver at 40 kW/m^2 seems reasonable: the fatigue damage due to the maximum number of cycles that can occur while guaranteeing the operation during the whole day is not particularly great –just slightly above the fatigue damage of the clear day- and, on the other hand, the creep damage is considerably reduced due to the drop of the receiver temperatures and stresses at such DNI. Additionally, to include the preheating conditions (case C) opposite to completely shut down the receiver (case D) helps reducing the fatigue damage. Nevertheless, in sight of the results obtained, setting a forecast window to decide whether to resume operation or not is advised as a good practice in order to reduce even more the fatigue damage.

As the result of the maximum creep and fatigue damages, the receiver lifetime is estimated for the three days individually, Figure 6, assuming the receiver would only work that way during its lifetime, in order to get an initial approximation on how these damages translate in terms of the receiver endurance. For a certain day, while the southern receiver panels have almost the same lifetime regardless the DNI case, divergences are observed in the northern ones, which happen to be the least enduring panels. Looking at these northern panels, the extreme fatigue scenario -and unrealistic for the best practice standards- results in the earliest receiver failure. Case C is the following one when looking at the first panel due to its high fatigue damage with respect cases A and B, although for the rest of the panels is similar to case B. Then, the clear-sky day is penalized by the high creep damage it must endure during the whole day, not benefitting from the descend on its temperatures and thermal stresses due to transient interruptions. Thus, the panels last longer throughout the whole receiver in case B, which suffers momentary descends in the creep damage but without presenting compromising fatigue levels. Nevertheless, the potential energy production would be lower than during the clear-sky conditions.

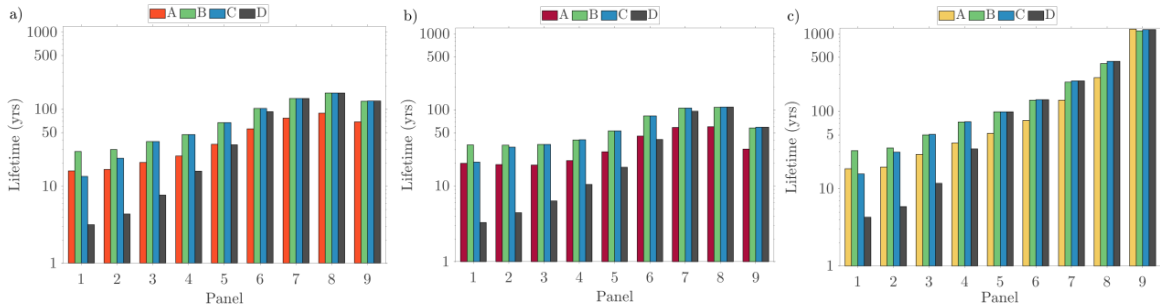

Fig 6: Lifetime estimation of the receiver panels considering the isolated damage contribution of a) day 81, b) day 172 and c) day 355.

Among the three days, the most critical in terms of creep damage is the spring equinox (see Figure 4), although it should be noted that, disregarding any potential limit set by the thermal storage system filling, the winter solstice presents an operation window over two hours shorter than the spring day. The summer solstice, being the day with the longest operation, suffers the lowest creep damage in the first receiver panel (the critical one the other two days), although it has the most damaged panels in terms of creep once passed the flow path half. The higher DNI of this day imposes the need to switch the aiming strategies earlier in the morning and later in the afternoon and thus, decreases the peak flux on the receiver, which explains why the creep damage is not that high despite operating two hours and a half more than the day 81 and over 4 hours and 40 minutes than day 355 during the clear-sky scenarios. The fatigue damage is very similar with the exception of the extreme fatigue case during the winter solstice, being slightly lesser.

5. Conclusions

This preliminary analysis of the damage mechanisms on a molten-salt solar central receiver during different transient conditions assumptions has the objective to test the receiver in critical conditions, from a day with an exceptional clear conditions to another one with high frequency fluctuations of its DNI.

It is observed that creep is the main damage mechanism even during days with small transients (case B) that allow a continuous operation, although the creep during low DNI periods could be considered negligible. Moreover, the additional fatigue damage caused by such small transients is barely noticeable since the fatigue damage comparison of cases A (clear-sky day) and B is highly resembling. From there, the fatigue damage increases with the amplitude of the strain, being advisable to keep the tubes preheating (case C) in order to avoid the excess of fatigue damage found when completely shutting down the receiver (case D), which would result in an excessively short receiver lifetime. The clear-sky assumption would be a conservative approach when obtaining the receiver lifetime due to the greater overall creep damage, while a quick calculation of the fatigue based on such clear-sky day could be admissible.

Overall, the results of the comparison carried out suggest that when keeping a reasonable control level of the receiver operation, as expected in any real facility of this kind, the creep dominates over the fatigue damage, even considering aspects such as the stress relaxation (relevant for the creep damage) or the tubes history and sample size (fatigue damage). It would be advisable to expand this preliminary study in future works, analyzing the creep/fatigue share under real DNI cases, implementing a DNI control on the receiver in order to start it up only according to its real necessities, so a more precise extent of the creep/fatigue share could be determined.

6. Acknowledgements

This research is partially funded by the scholarship “Ayudas para la formación del profesorado universitario” (FPU-02361) awarded by the Spanish Ministerio de Educación, Cultura y Deporte (MECD), the Spanish government under the project RTI2018-096664-B-C21 (MICINN/FEDER, UE) and the call “Programa de apoyo a la realización de proyectos interdisciplinares de I+D para jóvenes investigadores de la Universidad Carlos III de Madrid 2019-2020”, under the projects RETOrenovable-CM-UC3M and ZEROGASPAIN-CM-UC3M, funded on the frame of the Convenio Plurianual Comunidad de Madrid- Universidad Carlos III de Madrid.

7. References

American Society of Mechanical Engineers, 2010. ASME Boiler and Pressure Vessel Code, Section II Part D.

American Society of Mechanical Engineers, 1980. ASME Boiler and Pressure Vessel Code. Code Cases: Nuclear Components Code Case N-47.

Babcock & Wilcox Company, 1984. Molten Salt Receiver Subsystem Research Experiment Phase 1 -Final Report, Volume 1- Technical. Barberton, Ohio.

Barua, B., McMurtrey, M.D., Rupp, R.E., Messner, M.C., 2020. Design Guidance for High Temperature Concentrating Solar Power Components. https://doi.org/10.2172/1582656

Becht IV, C., 2011. Elevated temperature shakedown concepts. J. Press. Vessel Technol. Trans. ASME 133, 1–5. https://doi.org/10.1115/1.4003456

Berman, I., Gangadharan, A.C., Gupta, G.D., Narayanan, T. V, 1979. An interim structural design standard for solar energy applications. SAND79-8183. Albuquerque, New Mexico.

Burgaleta, J.I., Arias, S., Ramirez, D., 2011. Gemasolar, the first tower thermosolar commercial plant with molten salt storage, in: Proceedings of the SolarPACES 2011 Conference on Concentrating Solar Power and Chemical Energy Systems.

Chen, X., Sokolov, M.A., Sham, S., Erdman, D.L., Busby, J.T., Mo, K., Stubbins, J.F., 2013. Experimental and modeling results of creep-fatigue life of Inconel 617 and Haynes 230 at 850 °c. J. Nucl. Mater. 432, 94–101. https://doi.org/10.1016/j.jnucmat.2012.08.040

Conroy, T., Collins, M.N., Fisher, J., Grimes, R., 2018. Levelized cost of electricity evaluation of liquid sodium receiver designs through a thermal performance, mechanical reliability, and pressure drop analysis. Sol. Energy 166, 472–485. https://doi.org/10.1016/j.solener.2018.03.003

Falcone, P.K., 1986. A handbook for solar central receiver design. Livermore, CA. https://doi.org/10.2172/6545992

Fork, D.K., Fitch, J., Ziaei, S., Jetter, R.I., 2012. Life Estimation of Pressurized-Air Solar-Thermal Receiver Tubes. J. Sol. Energy Eng. 134. https://doi.org/10.1115/1.4007686

González-Gómez, P.A., Rodríguez-Sánchez, M.R., Laporte-Azcué, M., Santana, D., 2021. Calculating molten-salt central-receiver lifetime under creep-fatigue damage. Sol. Energy 213, 180–197. https://doi.org/https://doi.org/10.1016/j.solener.2020.11.033

Grossman, J.W., Jones, W.B., 1990. Evaluation of thermal cycling creep-fatigue damage for a molten salt receiver, ASME international solar energy conference, Miami, FL (USA).

Kistler, B.L., 1987. Fatigue analysis of a solar central receiver design using measured weather data. SAND86-8017. Albuquerque, New Mexico.

Laporte-Azcué, M., González-Gómez, P.A., Rodríguez-Sánchez, M.R., Santana, D., 2021a. Material selection for solar central receiver tubes. Sol. Energy Mater. Sol. Cells 231, 111317. https://doi.org/10.1016/J.SOLMAT.2021.111317

Laporte-Azcué, M., González-Gómez, P.Á., Rodríguez-Sánchez, M.R., Santana, D., 2020. Deflection and stresses in solar central receivers. Sol. Energy 195, 355–368. https://doi.org/10.1016/j.solener.2019.11.066

Laporte-Azcué, M., Rodríguez-Sánchez, M.R., González-Gómez, P.A., Santana, D., 2021b. Assessment of the time resolution used to estimate the central solar receiver lifetime. Appl. Energy 301, 117451. https://doi.org/10.1016/J.APENERGY.2021.117451

McConohy, G., Kruizenga, A., 2014. Molten nitrate salts at 600 and 680°C: Thermophysical property changes and corrosion of high-temperature nickel alloys. Sol. Energy 103, 242–252. https://doi.org/10.1016/j.solener.2014.01.028

Narayanan, T. V., Rao, M.S.M., Carli, G., 1985. Structural Design and Life Assessment of a Molten Salt Solar Receiver. J. Sol. Energy Eng. 107, 258–263. https://doi.org/10.1115/1.3267688

Neises, T.W., Wagner, M.J., Gray, A.K., 2014. Structural Design Considerations for Tubular Power Tower Receivers Operating at 650°C, in: Volume 1: Combined Energy Cycles, CHP, CCHP, and Smart Grids; Concentrating Solar Power, Solar Thermochemistry and Thermal Energy Storage; Geothermal, Ocean, and Emerging Energy Technologies; Hydrogen Energy Technologies; Low/Zero Emission Power Plants An. American Society of Mechanical Engineers, pp. 1–7. https://doi.org/10.1115/ES2014-6603

O. K., Chopra; W. J., S., 2003. Review of the margins for ASME code fatigue design curve – effects of surface roughness and material variability, Tech Rep NUREG/ CR6815, ANL-02/39. U.S. Nuclear Regulatory Commission.

Radke, E.F., Dewees, D.J., Wasyluk, D.T., Tanzosh, J.M., 2017. Creep-fatigue design applied to molten salt solar receivers, in: ASME 2014 Symposium on Elevated Temperature Application of Materials for Fossil, Nuclear, and Petrochemical Industries, ETAM 2014. pp. 232–247. https://doi.org/10.1115/ETAM2014-1032

Reno, M.J., Hansen, C.W., Stein, J.S., 2012. Global horizontal irradiance clear sky models : implementation and analysis. Albuquerque, New Mexico. https://doi.org/10.2172/1039404

Rodríguez-Sánchez, M.R., Soria-Verdugo, A., Almendros-Ibáñez, J.A., Acosta-Iborra, A., Santana, D., 2014. Thermal design guidelines of solar power towers. Appl. Therm. Eng. 63, 428–438. https://doi.org/10.1016/j.applthermaleng.2013.11.014

Sánchez-González, A., Santana, D., 2015. Solar flux distribution on central receivers: A projection method from analytic function. Renew. Energy 74, 576–587. https://doi.org/10.1016/j.renene.2014.08.016

Vant-Hull, L.L., 2002. The role of "allowable flux density" in the design and operation of molten-salt solar central receivers. J. Sol. Energy Eng. Trans. ASME 124, 165–169. https://doi.org/10.1115/1.1464124